Embedded star clusters in the W51 giant molecular cloud

M. S. Nanda Kumar,[1]★ U. S. Kamath[2]★ and C. J. Davis[3]★

[1]*Centro de Astrofisica da Universidade do Porto, Rua das Estrelas, 4150-762 s/n Porto, Portugal*
[2]*Indian Institute of Astrophysics, CREST Campus, Shidlaghatta Road, Hosakote 562114, India*
[3]*Joint Astronomy Centre, 660 N. A'ohōkū Place, University Park, Hilo, HI 96720, USA*

ABSTRACT

We present sub-arcsecond (0.35–0.9 arcsec), near-infrared J-, H- and K-band photometric observations of six fields along the W51 giant molecular cloud (W51 GMC). Our observations reveal four new, embedded clusters and provide a new high-resolution (0.35 arcsec) view of the W51 IRS2 (G49.5 − 0.4) region. The cluster associated with G48.9 − 0.3 is found to be a double cluster enclosed in a nest of near-infrared nebulosity. We construct stellar surface density maps for four major clusters in the W51 GMC. These unveil the underlying hierarchical structure. Colour–colour and colour–magnitude diagrams for each of these clusters show clear differences in the embedded stellar populations and indicate the relative ages of these clusters. In particular, the clusters associated with the H II regions G48.9 − 0.3 and G49.0 − 0.3 are found to have a high fraction of young stellar objects and are therefore considered the youngest of all the near-infrared clusters in the W51 GMC. The estimated masses of the individual clusters, when summed, yield a total stellar mass of $\sim 10^4$ M$_\odot$ in the W51 GMC, implying a star formation efficiency of 5–10 per cent. These results, in comparison with the CO observations of the W51 GMC, suggest for the first time that star formation in the W51 GMC is probably triggered by a galactic spiral density wave.

Key words: turbulence – stars: formation – ISM: clouds – H II regions – ISM: individual: W51 GMC – infrared: stars.

1 INTRODUCTION

W51 is classically known to be a complex of compact radio continuum sources representing a luminous star forming region in the Galactic disc. The λ21-cm maps show two major chunks of radio emission (representing complex H II regions) that are referred to as W51A and W51B. A diffuse and extended component of radio emission surrounding and extending to the east of W51B is called W51C and identified as a supernova remnant. The H II region complexes W51A and W51B are associated with intense molecular emission that is spread over an area of $1° \times 1°$ centred on $(l, b) \sim (49°.5, −0°.2)$. This large-scale molecular emission, which encompasses both W51A and W51B, is called the W51 giant molecular cloud (W51 GMC). Carpenter & Sanders (1998, hereafter CS98) present CO $J = 1$–0 and ^{13}CO $J = 1$–0 maps of the W51 GMC and show that all of the bright, compact H II regions are situated along a high-velocity cloud which they identify as a '68 km s^{-1}' cloud. Koo (1999) present higher resolution maps of the W51B region in CO $J = 2$–1 and 1–0 emission. CS98 argue

that W51 is in the top 1 per cent of all Galactic molecular clouds by size, and is in the top 5–10 per cent by mass.

To describe this complex region better in the context of the work presented here, we show in Fig. 1 a multi-wavelength view of the W51 GMC. The top panel shows contours of the λ21-cm radio continuum image from Koo & Moon (1997) overlaid on a grey-scale 8-μm emission image obtained by the *MSX* mission. The radio continuum sources (filled triangular symbols) G49.4 − 0.3 and G49.5 − 0.4 are referred to as W51A and the remaining components, namely G49.2 − 0.3, G49.1 − 0.4, G49.0 − 0.3 and G48.9 − 0.3, constitute the W51B region. Mehringer (1994) used high-resolution radio continuum and recombination line observations to identify several components of the H II regions associated with the W51 complex. Following his nomenclature, G49.5 − 0.4, the most luminous source in W51, is resolved into at least eight components (W51a–h). The most prominent among these are W51d and W51e which correspond to the strong infrared sources IRS2 and IRS1 (Goldader & Wynn-Williams 1994) respectively.

Fig. 1(b) (bottom panel) displays ^{13}CO $J = 1$–0 emission contours of the 68 km s^{-1} cloud (CS98) overlaid on a 2MASS K-band image mosaicked by us. Comparison of Figs 1(a) and (b) shows that while the H II regions of W51A are fairly well enclosed by the observed ^{13}CO emission, the W51B H II regions extend beyond the densest regions of the molecular cloud, traced in 8-μm emission.

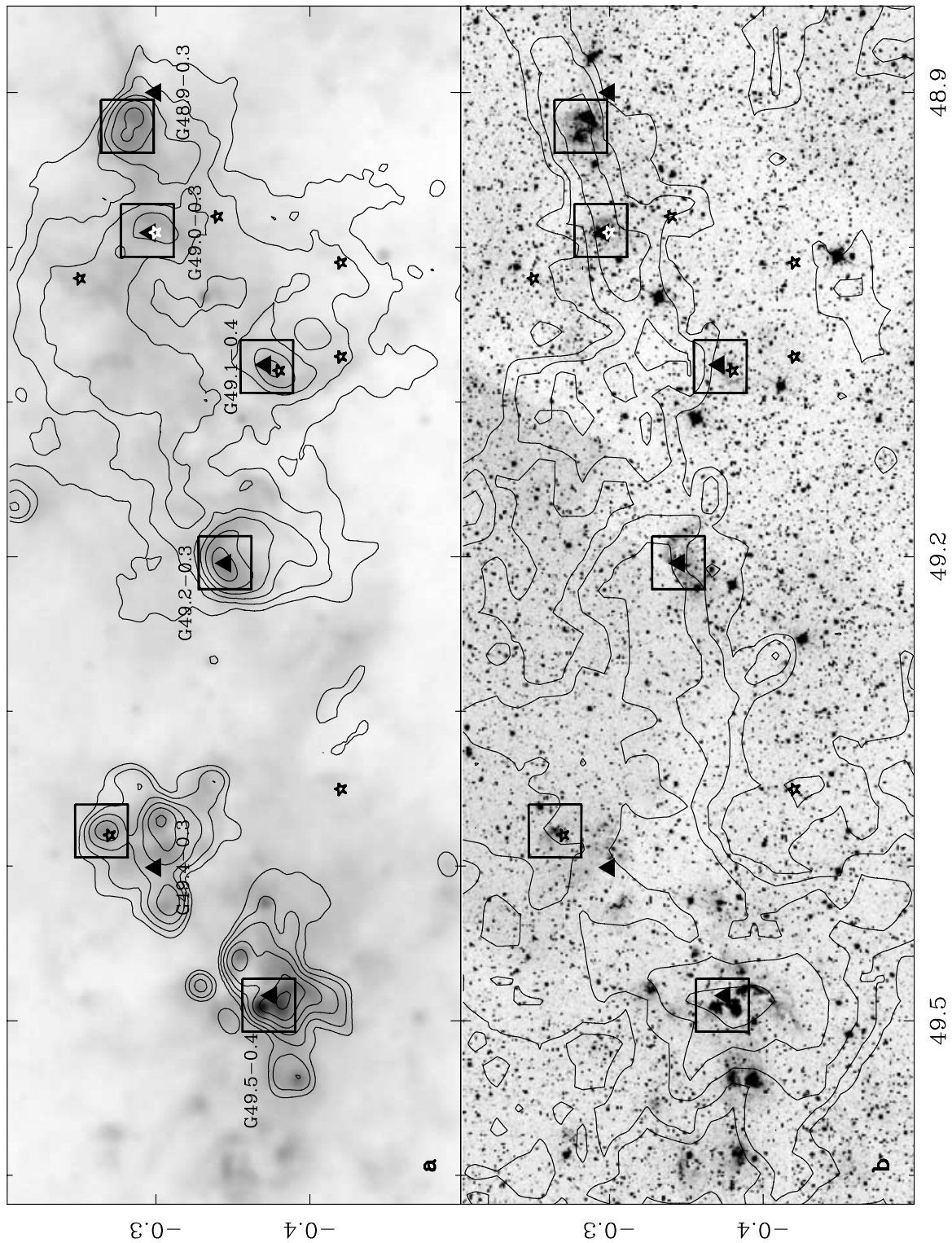★E-mail: nanda@astro.up.pt (MSNK); kamath@crest.ernet.in (USK); cdavis@jach.hawaii.edu (CJD)

Figure 1. (a) *MSX* A-band (8 μm) image of the W51 GMC, displayed on a logarithmic scale, overlaid by 21-cm continuum contours (Koo & Moon 1997). The contour levels are 0.1, 0.2, 0.4, 0.8 and 1.6 Jy beam^{-1}. (b) 2MASS *K*-band image of the same region overlaid by contours of ^{13}CO integrated intensity (CS98). Contour levels are 8, 16, 32 and 64 K km s^{-1}. The square boxes mark the observed regions, triangular symbols show the positions of associated UCHII regions and the star symbols represent the *IRAS* sources that satisfy the Wood & Churchwell (1989) criteria.

The mid-infrared *MSX A*-band image, which traces emission from the large-scale warm dust, resembles the 2MASS *K*-band image, which traces the embedded stellar content and hottest regions of gas and dust, in two ways. The extended, whitish regions in the 2MASS image (see also the atlas image of W51 on the 2MASS web site[1]), which are caused by extinction of the background light, coincide with the brighter regions (darker shades) in the *MSX* image. However, these regions also coincide with *compact* clusters of stars in the 2MASS image. Further, these condensations are also traced by the radio continuum emission, which delineates the H II regions and therefore the ionized gas. As is evident from Fig. 1(b), all of these bright condensations, which represent luminous star-forming regions, are situated along the 68 km s^{-1} cloud. This indicates that they may be embedded in this GMC. A cursory study of the 2MASS data shows that the regions enclosed by the bold, square boxes in Fig. 1 probably host embedded clusters. This has prompted the observations discussed in this paper, where we present high spatial resolution near-infrared (NIR) photometric studies of the regions marked with the boxes in Fig. 1. However, this is not a complete sample, because there are a few other unstudied objects appearing in the 2MASS image that look quite similar to the regions of our choice. The following results provide a new picture of large-scale star formation in the W51 GMC, which was not clear from previous studies that mostly concentrated on the W51A region.

2 OBSERVATIONS AND DATA REDUCTION

NIR observations were made at the 3.8-m United Kingdom Infrared Telescope (UKIRT) with the facility imager UFTI. The UFTI pixel scale measures 0.091 arcsec; the available field of view is ∼90 arcsec. Photometric observations through *JHK* broad-band filters were secured for six fields during three nights of service observing (2000 September 15, 2001 May 31 and 2001 August 12). Total exposure times in the *J*, *H* and *K* filters were 180, 180 and 360 s respectively on each of the target fields. The seeing varied between 0.32 and 0.9 arcsec with a mean of 0.5 arcsec in the *K* band for the photometric data. A nine-point (3 × 3) jittered observing sequence was executed to obtain data that provided final mosaics with a total field of view of ∼115 × 115 arcsec^2. We note that the signal-to-noise ratio at the edges of these mosaics is lower than that within the central 90-arcsec area. Standard data reduction techniques involving dark subtraction and median sky flat-fielding were applied.

We used tasks available under IRAF for photometric analysis. DAOFIND was used to identify sources in each image. A threshold equal to four times the mean noise of each image was found to be sufficient for this purpose. A point spread function (PSF) model was computed by choosing several bright stars well spaced out in the image. Photometry was performed using DAOPHOT. Aperture corrections were determined by performing multi-aperture photometry on the PSF stars. The instrumental magnitudes were calibrated to the absolute scale using observations of UKIRT faint standards (FS29, FS35 and FS149) that were obtained at airmasses closest to the target observations. The resulting photometric data are in the natural system of the Mauna Kea Consortium Filters (Simons & Tokunaga 2002). For the purposes of plotting these data in Figs 4 and 5 (later) we have converted them to the Bessell & Brett (1988) (BB) system, since the main-sequence references are in the BB system. Since the direct transformation equations between the Mauna Kea system and the BB system are not established as of now, we first converted the Mauna Kea system to the California Institute of

Technology (CIT) system and then to the BB system using equations given by Hawarden et al. (2001). We note that this indirect method can induce high errors for extremely red objects. Representative sub-images of G48.9 − 0.3 and G49.5 − 0.4, consisting of stars and nebulosity, were chosen for determination of the completeness limits. Limits were established by manually adding and then detecting artificial stars of differing magnitudes. By determining the fraction of stars recovered in each magnitude bin, we have deduced 90 per cent completeness limits of 18.2, 16.9 and 17.3 in the *J*, *H* and *K* bands respectively. Our observations are absolutely complete (100 per cent) to the level of 16.2, 14.4 and 15.8 mag in *J*, *H* and *K* respectively. The relatively higher detection level in *K* is due to the fact that the exposure times were twice those in the *J* and *H* bands. The photometric accuracy of data presented here is generally < 0.2 mag, although more than 30 per cent of the data points presented in electronic tables have magnitude errors less than 0.05 mag. Astrometry for each of the images was calibrated by using the 2MASS as reference. The astrometric accuracy of the data presented in this paper is better than 0.5 arcsec.

3 EMBEDDED CLUSTERS IN THE W51 GMC

We imaged six fields along the W51 GMC as represented by the bold, square boxes in Fig. 1. Fig. 2 displays *JHK*-band three colour composites of each of the observed fields. Regions are referred to using the nomenclature of the associated ultracompact H II (UCHII) region. The images are displayed on a linear scale except for the field G49.5 − 0.4 which is shown with a logarithmic scale to reveal the central region. As can be seen from Fig. 2, five of these six fields possess clusters of stars immersed in *K*-band nebulosity. The definition of a cluster here implies (1) a significant increase in the stellar density with respect to an adjacent background, and (2) association with radio continuum sources. The field around G49.5 − 0.4 is associated with the clusters known as W51 IRS1 and IRS2 (Goldader & Wynn-Williams 1994). The remaining four clusters are newly discovered from the observations presented here. The star symbols in Fig. 1 mark the positions of *IRAS* sources that satisfy the Wood & Churchwell (1989) criteria for UCHII regions. Three of these *IRAS* sources are associated with embedded clusters; the remaining ones are not associated with any NIR counterparts. The geometrical coincidence of the observed clusters with the ^{13}CO contours and the 21-cm contours indicates that these regions are 'embedded' in the gas and dust of the W51 GMC. Table 1 summarizes the positions and statistics for the five fields, derived from our *JHK*-band photometric analysis. These numbers do not reflect the actual number of stars that belong to the clusters. Our photometric observations provide statistically meaningful data for only four of the five observed clusters; we therefore present detailed analysis only for these four clusters. The regions of G49.4 − 0.3 and G49.1 − 0.4 are not included in the detailed analysis presented below.

3.1 Notes on individual clusters

The four embedded clusters discussed below are associated with bright far-infrared (FIR) and radio continuum emission. They are, in their own right, interesting objects for detailed high-resolution studies at various wavelengths.

3.1.1 G49.5−0.4

This H II region complex is composed of two major components known as W51d and W51e, which are associated with two embedded clusters identified by the prominent infrared sources IRS2 and IRS1 (see Fig. 1) The brightest region, W51d, is well studied

Figure 2. *JHK* colour composites of W51 embedded clusters.

Table 1. Summary of observed fields.

Name	Coordinates (J2000)		PSF arcsec	Number of Stars			
	RA	Dec.		*J*	*H*	*K*	*JHK*
G48.9 − 0.3	$19^h22^m14^s$	$14° 03'09''$	0.36	662	1359	2071	593
G49.0 − 0.3	$19^h22^m26^s$	$14° 06'46''$	0.50	954	1659	1757	702
G49.2 − 0.3	$19^h23^m02^s$	$14° 16'41''$	0.90	469	882	905	293
G49.4 − 0.3	$19^h23^m05^s$	$14° 28'07''$	1.10	542	702	744	304
G49.5 − 0.4	$19^h23^m40^s$	$14° 31'07''$	0.32	651	977	1865	529

at centimetre, millimetre and infrared wavelengths. W51d/IRS2 is now known to be a young embedded star cluster which is larger and more luminous than the Orion–Trapezium cluster. It contains the water maser complex W51N (Forster & Caswell 1989) and several OH and SiO maser sources (Caswell 2003; Fish et al. 2003), and is thought to contain several O-type young stars. In Fig. 2, the inset of the G49.5 − 0.4 panel shows a three-colour *JHK* composite image of the central region of the W51d/IRS2 cluster which, at a spatial resolution of 0.32 arcsec, reveals more details than any other image of this region obtained until now. The region shows bright stars and nebulosity, the nebulous cloud appearing to be pinched off to form two lobes stretched east–west. These are called IRS2E and IRS2W and are shown to have electron densities of 10^5–10^6 cm^{-3} (Okumura et al. 2001). Our observations show that IRS2E is associated with a dense cluster, while IRS2W is relatively devoid of stars. Further, the high-resolution view suggests that IRS2E and IRS2W are probably two massive star-forming clumps bound by a Roche lobe potential. The central region is associated with 6–7 mid-infrared point sources (Kraemer et al. 2001; Okamoto et al. 2001), six of which appear as point sources in our high-resolution NIR image. One of the sources appears as a red nebulous condensation (the brightest star of the western blob in the inset) and corresponds to the source KJD3 (Kraemer et al. 2001) which is known to be associated with deep silicate absorption features. Most of these mid-infrared sources are thought to be O-type stars, although there is some debate about whether they are O5–O6 or O9-type stars (Okamoto et al. 2001).

3.1.2 G48.9−0.3

This source is associated with one of the most spectacular clusters discovered in the W51 GMC. The top right panel in Fig. 2 displays the three-colour composite of this newly discovered embedded cluster. This cluster is located towards one edge of the ∼100 pc long 68 km s^{-1} molecular cloud. It appears to be placed on the tip of the molecular cloud and the observed H II region W51B. High-resolution ISOCAM data for this region show strong FIR emission at 6 μm with a morphology similar to that of the 8-μm *MSX* data shown in Fig. 1. This is a twin cluster immersed in a cradle of nebulosity visible at NIR wavelengths. The southern sub-cluster is a centrally symmetric cluster with a bright white/blue star situated at the geometric centre. In contrast, the northern sub-cluster does not have a prominent source, although it does appear centrally symmetric. Indeed, here there appears to be a small ring of stars that is orientated in the plane of the sky.

3.1.3 G49.2−0.3

This is the strongest UCHII region found in the W51B region and corresponds approximately to the location where the shock from the W51C supernova remnant is thought to be interacting with the W51 GMC (Koo & Moon 1997). It is associated with a group of bright red stars located at the boundary of a cometary-shaped H II

region. The *K*-band (red) nebulosity has a similar morphology and is found to be well aligned with the radio free–free emission shown in Fig. 1. Unfortunately, our photometric data for this region suffer from relatively poor seeing (0.9 arcsec) and a tracking error which does not allow us to resolve effectively the otherwise dense group of faint sources that is enclosed by the cometary-shaped H II region.

3.1.4 G49.0-0.3

The bottom right panel of Fig. 2 shows the three-colour composite of this field. This region of the W51 GMC is bright at 6–8 μm and is relatively weak in terms of radio continuum emission, probably indicating a younger cluster and weaker H II region in comparison with other brighter sources in the W51B region. A faint 'bow' of *K*-band nebulosity, which is similar in morphology to the associated radio continuum emission, surrounds the cluster. This is probably a photodissociation region. Our three-colour image shows a bright red star centrally located in the cluster. Also found are two knots of *K*-band (red) nebulosity in the central region that cannot be easily related to any particular star.

3.2 Spatial distribution of stars

It is evident from Fig. 1(b) that the spatial distribution of near-infrared sources is non-uniform, on the global scale of the GMC and also on the local scale of the individual clusters. In order to study the nature of this distribution it is necessary to construct star count surface density maps (SDMs). Such maps provide quantitative estimates of stellar surface densities and their variation across the clusters. They also reveal details about the nature of star formation and the hierarchical structure. Different methods of generating such maps have been followed in various studies of nearby young star clusters. While Lada & Lada (1995) use overlapping rectilinear grids of boxes separated by Nyquist criteria to count the sources in the IC 348 cluster, Hillenbrand & Hartmann (1998) bin the source counts into 10-arcsec pixels and smooth the resulting map with a symmetric Gaussian profile with a 3-pixel width to produce stellar surface density maps of the Orion nebula cluster.

In the above cases the targets of study were nearby star-forming regions within 500-pc distance where meaningful source counts could be obtained over projected angular areas of several square arcminutes. Massive star-forming regions like W51 are generally at much larger distances and thus subtend relatively small angular sizes, making it difficult to study star count distribution. In these cases spatial resolution plays an important role in the extraction of meaningful information from the SDM. The sizes of individual features that we may expect to see on the SDMs depends on the full width to half-maximum (FWHM) of the point spread function (PSF), the binning size adopted to generate the SDMs and the count level itself. Together, these determine whether or not a meaningful SDM can be made. The binning size is a smoothing factor that has to be carefully chosen in such a case. While a small bin size can include just a few sources and not provide a meaningful SDM, an overly large bin size can hide the true features in the SDMs. Given the high quality of the seeing (0.32 arcsec) in the *K*-band images of two fields, we experimented with different bin sizes corresponding to 6, 9, 12, 15, 18 and 22 times the FWHM of the PSFs. We found that, while the majority of identifiable features did not vary significantly between 6 and 12 times FWHM, the features began to get smeared for a bin size larger than 12 times FWHM. However, to identify the boundaries of the overall cluster and estimate its physical characteristics, a much larger bin size, to smooth all the features, had to be employed.
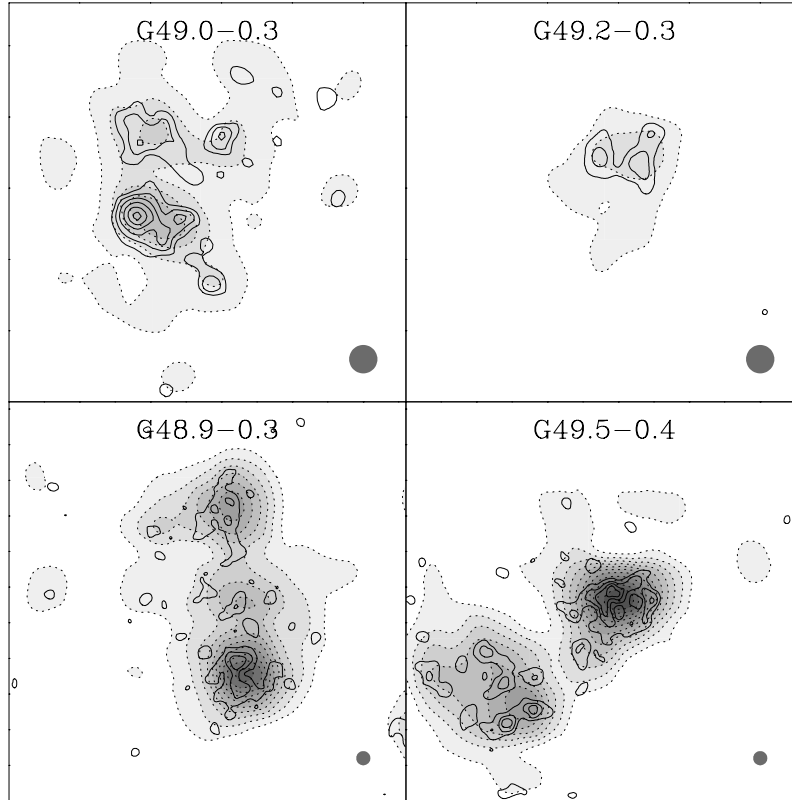
Figure 3. Stellar surface density contours generated by Nyquist binning *K*-band star counts. The dotted curves with grey shades represent the boundaries of the clusters and are obtained by using a bin width of 7 arcsec. The levels of the dotted contours begin at 4 stars per pixel (7 arcsec) and increase in steps of 2 stars per pixel. The solid curves represent the hidden structure of these clusters and are revealed by using smaller bin widths represented by the grey circles in each panel.

In Fig. 3 we show SDMs for four fields where the detected source counts were sufficient to produce such a map. We have adopted the method of Lada & Lada (1995), who use a rectilinear grid of overlapping squares separated by half the width of individual squares to provide Nyquist sampling of the sources. We counted all sources from the *K*-band photometry within our completeness limits discussed in the previous section. The cut-off *K* magnitude for this choice was 17.8 (85 per cent detection limit); the magnitude errors were less than 0.3 mag. The dotted contours and grey shades in Fig. 2 indicate the source distribution as obtained by a large smoothing box (150 pixel ∼14 arcsec). These contours are used to identify the cluster boundaries and estimate the average surface density of each cluster. The thick contours overlaid on the grey shades represent SDMs generated by using a smaller bin size (14 × PSF) that that shows smaller groups within these clusters. All four clusters reveal a clumpy distribution of the NIR sources, and the clumps are found to be either elliptical or circular in shape. The elliptical clumps are particularly noticeable in the maps of G48.9−0.3 and G49.5−0.4. The projected dimensions of these clumps are approximately 0.1–0.2 pc. Using the SDM generated with large bins (smooth maps), we estimated the number of stars and the stellar surface densities for each cluster.

4 COLOUR–COLOUR (CC) AND COLOUR–MAGNITUDE (CM) DIAGRAMS

Table 1 lists the number of stars detected in each of the *J*, *H* and *K* photometric bands, and simultaneously in all three

bands, for each of the fields. For the purposes of photometric analysis of the clusters, we chose all those stars with photometric errors less then 0.2 mag. Tables 2–5 (available electronically only, at http://www.blackwellpublishing.com/products/journals/suppmat/mnr/mnr8143/mnr8143sm.htm) list the astrometry (RA, Dec.) and photometry (magnitudes and errors for each of the *J*, *H* and *K* bands) of the stars in sources G48.9 − 0.3, G49.0 − 0.3, G49.2 − 0.3 and G49.5 − 0.4 respectively. For the four clusters with SDMs in Fig. 3, the stars detected in all three photometric bands are plotted on *JHK* colour–colour (CC) diagrams in Fig. 4. The solid and broken heavy curves represent the main-sequence dwarf and giant stars, respectively, and the dashed parallel lines are the reddening vectors that enclose reddened main-sequence objects. Okumura et al. (2000) estimated the slope of the reddening vector in the direction of W51 to be ∼1.9. Similar results are obtained by using 2MASS data. We therefore assumed a reddening vector slope $E(J − H)/E(H − K) = 1.9$ (BB system) towards the W51 region, which relates to an interstellar reddening law with a value of $R = 3.12$ (Whittet & van Breda 1980). The dotted line indicates the locus of T Tauri stars (Meyer, Calvet & Hillenbrand 1997) and the dotted curve represents the HAeBe locus (Lada & Adams 1992). Stars that lie outside the region of reddened main-sequence objects are young stellar objects (YSOs) with intrinsic colour excesses. By dereddening the stars (on the CC diagrams) that fall within the reddening vectors encompassing the main-sequence stars and giants, we found the visual extinction to each star. We dereddened the stars to the K6–M6 part of the sequence of stars. The individual extinction values range from 0 to 14 mag. From a histogram of
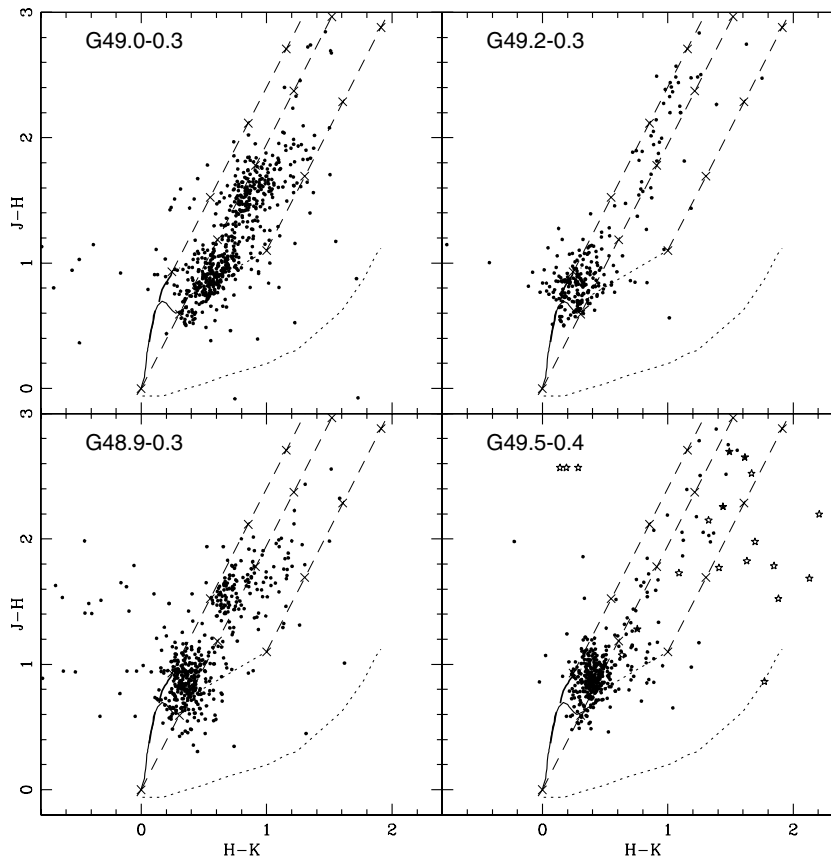
Figure 4. CC diagrams for four clusters. The solid and broken heavy curves represent the main-sequence dwarf and giant stars, respectively, and the dashed parallel lines are the reddening vectors that enclose reddened main-sequence objects. The crosses on the reddening vectors are separated by $A_v = 5$ mag. The dotted line indicates the locus of T Tauri stars (Meyer et al. 1997) and the dotted curve represents the HAeBe locus (Lada & Adams 1992). The star symbols in the bottom right-hand panel represent the sources in the W51 IRS2 region.

Table 6. Embedded clusters in the W51 GMC.

Name	Number of stars	Stellar density (pc^{-2}) Average	Peak	Radius (pc) ($\sqrt{A/\pi}$)	Age[a] Myr	A_v mag	Mass[b] M$_\odot$
G48.9 − 0.3	658	175	475	3.43	1.4	5,10	10 000
G49.2 − 0.3	505	130	250	3.48	3.0	6,11	8000
G49.4 − 0.3	148	123	175	1.95	2–3	5	2000
G49.5 − 0.4 (IRS1D)	309	221	535	2.09	0.7	5	4400
G49.5 − 0.4 (IRS1E)	333	179	340	2.39	0.7	5	4700

[a]Age of associated H II region.
[b]Calculated for an age of 1 Myr and $A_v \sim 7$ mag.

these values, we estimate the average foreground extinction to each of the clusters. Two of the clusters (G48.9 − 0.3 and G49.0 − 0.3) show two prominent peaks of extinction on the histogram corresponding to the two groups of points that can be identified on the CC diagram. The estimated values of extinction are listed in Table 6.

It can be noted from Fig. 4 that there are significant differences between the stellar populations of the four clusters. G49.0 − 0.3 and G48.9 − 0.3 shows two distinct groups of points on the CC diagram separated by about 5–10 mag of visual extinction. In contrast, G49.2 − 0.3 and G49.5 − 0.4 do not show such distinct groups. Nearly 90 per cent of the points that belong to G49.0 − 0.3 lie in the region of intrinsically reddened objects, thus signifying a high fraction of YSOs. Further, it appears that G49.0 − 0.3 has two groups of YSOs, one group more reddened than the other. We found that these

two groups of YSOs are distributed homogeneously over the cluster area. Thus the more reddened group is probably embedded in the molecular clump while the least reddened group is probably partially out of or in front of the clump. The bright red star in G49.0 − 0.3 (see Fig. 2) at the centre of the cluster shows colours similar to a T Tauri star and is highly reddened ($A_v \sim 35$ mag). This could be a massive star embedded in this cluster-forming core.

In G48.9 − 0.3 there is a good mixture of both main-sequence and YSO populations. However, unlike G49.0 − 0.3, the two groups in this case are found to be distributed differently. The reddened group of stars are all found to occupy the central parts of the two (northern and southern) sub-clusters (see Fig. 2), while stars without much reddening are found to be distributed over the entire field of view of the image. Therefore the average extinction value derived from the reddened group of stars is a good representation
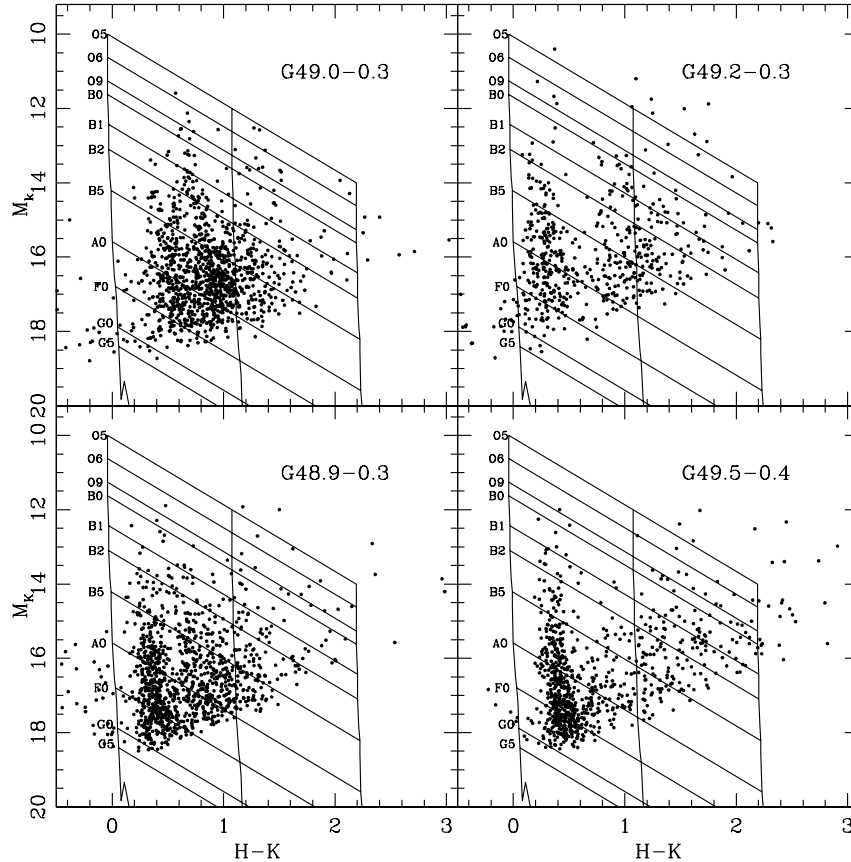
Figure 5. CM diagrams for four fields. The vertical solid lines (from left to right) represent the main-sequence curve reddened by 0, 20 and 40 mag respectively. The horizontal parallel lines represent reddening vectors.

of the visual extinction to the molecular clump that hosts the two clusters.

The G49.5 − 0.4 CC diagram shows mostly main-sequence objects. There is a small percentage of YSOs with varying degrees of reddening. The star symbols in Fig. 4 mark the positions of the stars associated with IRS2 (which is shown inset in the bottom left-hand panel in Fig. 2). These stars are thought to be O-type stars. The placement of these sources in the upper right-hand part of the CC diagram supports the conjecture that these are indeed O-type stars (Lada & Adams 1992). Finally, in Fig. 4 G49.2 − 0.3 displays very few YSOs and only a few reddened main-sequence objects. If we consider the ratio of sources that fall in the main-sequence zone and the YSO zone as an indicator of the cluster age, then the differences in the CC diagrams discussed above imply that G49.0 − 0.3 is the youngest cluster in W51, while G48.9 − 0.3 is the second youngest cluster. In comparison, G49.5 − 0.4 and G49.2 − 0.3 are relatively evolved objects.

Fig. 5 shows K versus $H − K$ colour–magnitude (CM) diagrams for all four clusters. The vertical solid lines (from left to right) represent the main-sequence curve reddened by 0, 20 and 40 mag respectively. We have assumed a distance of 6.5 kpc for all the clusters, and respective A_v values (listed in Table 1) to each cluster in order to reproduce the main-sequence data appropriately on this plot. Similarly to the CC diagrams, the CM diagrams show clear differences between the four clusters. The reddened main-sequence stars are found to be spread parallel to the main-sequence line. Clusters G49.5 − 0.4, G48.9 − 0.3 and G49.2 − 0.3 clearly display this concentration of main-sequence points, which is almost completely

absent in the G49.0 − 0.3 cluster. This agrees well with the results from the CC diagram for G49.0 − 0.3, i.e. that YSOs comprise about 90 per cent of the total membership of this cluster. The CM diagram of G48.9 − 0.3 shows the YSOs and main-sequence stars to be well separated. Points that lie in the upper right-hand corner of the CM diagram (above the line corresponding to O5) represent good candidates for massive YSOs. The relative numbers of such points are highest in G49.5 − 0.4, followed by G49.2 − 0.3 and G48.9 − 0.3. In contrast, G49.0 − 0.3 has almost all of its points concentrated in the lower right-hand corner of the CM diagram, corresponding to a population of essentially low-mass stars. However, an estimation of the true spectral type of each star cannot be made using the CM diagram alone, and warrants NIR spectroscopic observations of the individual sources.

5 DISCUSSION

5.1 Estimating cluster properties

In Table 6 we summarize some of the estimated properties of the four embedded clusters in the W51 GMC. These estimates are based on the photometric analysis presented in previous sections and some standard methods. The clusters and their boundaries were identified using the SDMs shown in Fig. 3. The stars that fall within the outermost contours shown in Fig. 3 (dotted contours and grey shades) were counted to estimate the number of stars in the cluster. However, the stellar surface densities (average and peak values) were estimated by using the star counts within the contour equal to half the peak value. It is clear from Fig. 3 that the clusters are not

circularly symmetric and indeed have irregular clumps. The projected areas of the clusters were used to define an equivalent radius for the cluster as $R = \sqrt{A/\pi}$, where A is the estimated area of each cluster from Fig. 3. We have estimated a mass for each cluster based on the method described by Lada & Lada (2003). Following this method, we have assumed the K-luminosity function (KLF) models of the Orion Trapezium cluster (Muench et al. 2002) as a template and used the evolutionary tracks of D'Antona & Mazzitelli (1994) in computing the estimated masses. We have used an age of 1 Myr, a distance of 6.5 kpc and an average foreground extinction of $A_v \sim$ 7 mag to compute the masses. The effect of age on the mass of the cluster is such that ages $\leqslant$ 1–2 Myr yield lower masses compared with ages $\geqslant$ 1–2 Myr, with all other parameters fixed. However, these assumptions are fair, given the uncertainties involved in our assumed parameters. The estimated mass for the G49.5 − 0.4 region (IRS1 and IRS2) together is 9100 M$_\odot$ which is similar to the mass estimated by Okumura et al. (2000) for this region (8200 M$_\odot$) assuming a Salpeter mass function. Our higher estimate is as expected because the spatial sampling here is a factor of 5–6 better compared with Okumura et al. (2000), thus revealing a larger number of cluster members. We also note that the estimated masses are quite sensitive to the assumed extinction values, particularly for distant sources such as these. Therefore the estimated masses can be uncertain by a few thousand solar masses.

The age of a cluster is one of the most difficult parameters to estimate with our present knowledge because of both observational difficulties and theoretical uncertainties [see Lada & Lada (2003) for a discussion of this problem]. In the case of massive star-forming regions, some authors use the age of the associated H II regions as an indication of the age of the associated groups of stars. For example, Okumura et al. (2000) give such ages for the four regions falling in the region of W51A. Extending this method to the entire W51 GMC region, one finds that the G48.9 − 0.3 is older than G49.5 − 0.4 (IRS2). From the studies presented here, if we consider the ratio of YSOs to main-sequence stars in each cluster as an indicator of its youth, and also consider the ages indicated by the CM diagrams, it turns out that the IRS2 region is older than the G48.9 − 0.3 region. This contradicts the result obtained by comparing the ages of the H II regions. It has been suggested that the UCHII region phases of massive stars last for a time period much longer than 10^5 yr if they are born in dense and hot regions (de Pree, Rodriguez & Goss 1995). This is because the pressure exerted by the surrounding environment holds the expansion of the UCHII region phase. It may even be possible that massive star formation took place at a much later stage than the low-mass star formation (Herbig 1962; Stahler 1985). Therefore, neither the ages of the massive YSOs nor the ages of the associated H II regions are good indicators of the age of the associated embedded clusters.

5.2 Hierarchical and triggered star formation in the W51 GMC

The studies presented here indicate the existence of at least two, and possibly three, levels of hierarchy in the W51 GMC. From Fig. 1 it is evident that star formation has occurred in two major clumps, known as W51A and W51B, within a ∼100 pc long molecular cloud. These clumps need not be real and could indeed be the effect of disruption by the supernova remnant W51C [see Koo & Moon (1997) for a detailed discussion]. The infrared image of the W51A region shows several clumps that are found as associations of stars and nebulosity (see fig. 1 of Hodapp & Davis 2002). Next, as seen in Fig. 2, there is clustering within each of the four clusters. In particular, if we con-

sider the example of G48.9 − 0.3, which is a double cluster, there appears to be an additional level of hierarchy. All of the clusters, at various levels, indicate hierarchical clustering. Hierarchical structure is believed to be a direct consequence of turbulent energy that operates similarly at different scales [see e.g. reviews by Elmegreen et al. (2000) and Mac Low & Klessen (2004)]. Thus the observed hierarchical clustering indicates the presence of significant turbulent energy in the W51 GMC which is not yet dissipated. The observed star formation has therefore taken place in the presence of strong turbulent energy.

If we sum up the mass of all of the clusters listed in Table 6 we find a total stellar mass of ∼ 30 000 M$_\odot$. Our observations probably represent only ∼50 per cent of the total star formation in the W51 GMC, for various reasons. First, we have not sampled all the smaller associations/clusters that can be seen in a large-scale 2MASS K-band image. Next, our observations have poor spatial resolution for two of the major clusters; this results in an overly undersampled cluster membership for each cluster. Also, the distributed component of individual young stars across the cloud can contribute a significant percentage to the stellar mass which is neglected. Thus the total mass estimates from these clusters alone are lower limits. In view of these uncertainties, it may not be unreasonable to assume that the overall star formation in the W51 GMC is associated with a mass of ∼5–6 × 10^4 M$_\odot$. In such a case, the estimated mass of the W51 GMC, ∼10^6 M$_\odot$, derived from observations of the molecular cloud itself (CS98), implies a star formation efficiency (ratio of stellar mass to cloud mass) of ∼5–6 per cent. CS98 showed that four of the radio continuum sources, namely G48.9 − 0.3, G49.0 − 0.3, G49.1 − 0.4 and G49.2 − 0.3, are spatially and kinematically associated with the 68 km s^{-1} cloud alone. If we believe that all the observed clusters in the W51 GMC do indeed belong to the 68 km s^{-1} cloud, then the mass estimate of ∼2 × 10^5 M$_\odot$ for the 68 km s^{-1} cloud (CS98), together with the mass estimates for the clusters in Table 6, indicates star formation efficiencies ∼10–15 per cent. This value is comparable to the star formation efficiencies in some relatively nearby massive star-forming clusters, such as NGC 6334 (25 per cent, Tapia, Persi & Roth 1996) and W3 IRS5 (6–18 per cent, Megeath et al. 1996).

Low-mass star formation in the solar neighbourhood is known to have a low efficiency, of the order of 1–3 per cent. Triggering mechanisms are thought to result in the formation of clusters; they are also thought to be associated with higher star formation efficiencies. In the W51 GMC, the embedded clusters are distributed inside a ∼100 pc long cloud. The clusters also probably have ages of 0.5–3 Myr because these are the commonly observed ages of observed embedded clusters (Lada & Lada 2003). This suggests near-simultaneous star formation across the entire cloud, an event which could have been spontaneous and/or triggered by an external mechanism. If a triggering mechanism was involved then it would have to have been a large-scale shock wave to influence the 100 pc long region. Internal trigger mechanisms are very unlikely in this case, since the crossing time for the cloud, for an average velocity of ∼10 km s^{-1}, is ∼10 Myr, which is larger than the typical lifetime of 3–5 Myr for the embedded clusters. When we consider these facts and note the location of the W51 GMC at the tangent point of the Sagittarius spiral arm (Burton 1970), it seems likely that the observed star formation in the W51 GMC is triggered by galactic spiral density waves. Giant clouds like W51 are indeed thought to undergo gravitational collapse under the influence of spiral density waves (Elmegreen 1994). Therefore the W51 GMC may be one of the best examples in our Galaxy of triggered star formation by spiral waves.

6 SUMMARY AND CONCLUSIONS

We present sub-arcsecond resolution, near-infrared *J*-, *H*- and *K*-band photometric observations of six fields in the W51 GMC (which includes the W51A and W51B regions). We construct a multi-wavelength view of the W51 GMC, combining CO and λ21-cm observations from the literature with *MSX* and 2MASS data. All of these observations together suggest a unified view for W51, the H II regions being associated with a $\sim$100 pc long molecular cloud named the '68 km s^{-1}' cloud by CS98. The results of our near-infrared observations can be summarized as follows.

(1) From our observations of six regions, four new, embedded clusters are discovered that are associated with the UCHII regions $G48.9 - 0.3$, $G49.0 - 0.3$, $G49.2 - 0.3$ and $G49.4 - 0.3$. Among these, the cluster associated with $G48.9 - 0.3$ is found to be a twin cluster enclosed in a nest of near-infrared nebulosity. Our observations also provide a sub-half-arcsecond view of the W51 IRS2 ($G49.5 - 0.4$) region which is known to be forming several O-type stars. This high-resolution image provides a view which suggests that W51 IRS2E and IRS2W are two massive star-forming clumps that are probably connected by a Roche lobe potential.

(2) Using *K*-band star counts, we construct stellar surface density maps for four clusters ($G48.9 - 0.3$, $G49.0 - 0.3$, $G49.2 - 0.3$ and $G49.5 - 0.4$.) These maps unveil the underlying hierarchical structure and allow us to estimate some physical parameters for the clusters. Colour–colour and colour–magnitude diagrams for each of the clusters indicate distinct differences in their embedded stellar populations. The clusters associated with $G48.9 - 0.3$ and $G49.0 - 0.3$ are found to contain a high percentage of YSOs, suggesting their relative youth in comparison to the other regions studied.

(3) Assuming an Orion Trapezium initial mass function and theoretical pre-main-sequence tracks, we estimate the masses of the individual clusters. The combined mass of all the clusters amounts to a net stellar mass of $\sim$10^4 M$_\odot$ in the W51 GMC. This estimate, when combined with estimates of the molecular cloud mass from CS98, suggests a star formation efficiency of $\sim$10 per cent.

Finally, the combined view of the W51 GMC, from our new observations and from the literature, suggests that star formation in the W51 GMC is probably triggered by a galactic spiral density wave. Thus W51 may represent a relatively unique example of massive star formation in our Galaxy.

REFERENCES

Bessell M. S., Brett J. M., 1988, PASP, 100, 1134
Burton W. B., 1970, A&AS, 2, 291
Carpenter J. M., Sanders D. B., 1998, AJ, 116, 1856 (CS98)
Caswell J. L., 2003, MNRAS, 341, 551
D'Antona F., Mazzitelli I., 1994, ApJS, 90, 467
de Pree C. G., Rodriguez L. F., Goss W. M., 1995, Rev. Mex. Astron. Astrofis., 31, 39
Elmegreen B. G., 1994, ApJ, 433, 39
Elmegreen B. G., Efremov Y., Pudritz R., Zinnecker H., 2000, in Mannings V., Boss A. P., Russell S. S., eds, Protostars & Planets IV. Univ. Arizona Press, Tucson, p. 179
Fish V. L., Reid M. J., Argon A. L., Menten K. M., 2003, ApJ, 596, 328
Forster J. R., Caswell J. L., 1989, A&A, 213, 339
Goldader J. D., Wynn-Williams C. G., 1994, ApJ, 433, 164
Hawarden T. G., Leggett S. K., Letawsky M. B., Ballantyne D. R., Casali M. M., 2001, MNRAS, 325, 563
Herbig G. H., 1962, ApJ, 135, 736
Hillenbrand L. A., Hartmann L. W., 1998, ApJ, 492, 540
Hodapp K. W., Davis C. J., 2002, ApJ, 575, 291
Koo B., 1999, ApJ, 518, 760
Koo B. C., Moon D. S., 1997, ApJ, 475, 194
Kraemer K. E., Jackson J. M., Deutsch L. K., Kassis M., Hora J. L., Fazio G. G., Hoffmann W. F., Dayal A., 2001, ApJ, 561, 282
Lada C. J., Adams F. C., 1992, ApJ, 393, 278
Lada C. J., Lada E. A., 2003, ARA&A, 41, 57
Lada E. A., Lada C. J., 1995, AJ, 109, 1682
Mac Low M., Klessen R. S., 2004, Rev. Mod. Phys., 76, 125
Megeath S. T., Herter T., Beichman C., Gautier N., Hester J. J., Rayner J., Shupe D., 1996, A&A, 307, 775
Mehringer D. M., 1994, ApJS, 91, 713
Meyer M. R., Calvet N., Hillenbrand L. A., 1997, AJ, 109, 1682
Muench A. A., Lada E. A., Lada C. J., Alves J. F., 2002, ApJ, 573, 366
Okamoto Y. K., Hirokazu K., Takuya Y., Takashi M., Takashi O., 2001, ApJ, 553, 254
Okumura S., Mori A., Nishihara E., Watanabe E., Yamashita T., 2000, ApJ, 543, 799
Okumura S., Mori A., Watanabe E., Nishihara E., Yamashita T., 2001, AJ, 121, 2089
Simons D. A., Tokunaga A., 2002, PASP, 114, 169
Stahler S. W., 1985, ApJ, 293, 207
Tapia M., Persi P., Roth M., 1996, A&A, 316, 102
Whittet D. C. B., van Breda I. G., 1980, MNRAS, 192, 467
Wood D. O. S., Churchwell E., 1989, ApJ, 340, 265

This paper has been typeset from a TEX/LATEX file prepared by the author.